Probing small neutron skin variations in isotope pairs by hyperon-antihyperon production in antiproton-nucleus interactions

Falk Schupp,[1] Josef Pochodzalla [●],[1,2,3,*] Michael Bölting,[1] Martin Christiansen [●],[1]
Theodoros Gaitanos [●],[4] Horst Lenske [●],[5] and Marcell Steinen [●][1]

[1]*Helmholtz-Institut Mainz, Johannes Gutenberg-Universität Mainz, D-55099 Mainz, Germany*
[2]*Institute für Kernphysik, Johannes Gutenberg-Universität Mainz, D-55099 Mainz, Germany*
[3]*PRISMA$^+$ Cluster of Excellence, Johannes Gutenberg-Universität Mainz, D-55099 Mainz, Germany*
[4]*Department of Theoretical Physics, Aristotle University of Thessaloniki, GR-54124 Thessaloniki, Greece*
[5]*Institut für Theoretische Physik, Justus-Liebig-Universität Gießen, D-35392 Gießen, Germany*

We propose a new method to study the evolution of the neutron periphery between different isotopes by considering antiproton-nucleus interactions close to the production threshold of $\Lambda\overline{\Lambda}$ and $\Sigma^-\overline{\Lambda}$ pairs. At low energies, $\Lambda\overline{\Lambda}$ pairs are produced in $\overline{p} + p$ collisions, while $\Sigma^-\overline{\Lambda}$ pairs can only be produced in $\overline{p} + n$ interactions. Within a simple geometrical picture we show that the double ratio for the production of $\Sigma^-\overline{\Lambda}$ and $\Lambda\overline{\Lambda}$ pairs for two different isotopes are related to the variation of the neutron skin thickness between the two nuclei. Performing high statistics calculations with the Gießen Boltzmann-Uehling-Uhlenbeck (GiBUU) transport model for several isotope pairs covering a wide range of elements, we verify a strong correlation between the double ratio from the full transport simulations and the schematic model. This correlation enables us to quantify the potential of the proposed method for precise studies of neutron skin variations in isotope chains.

I. INTRODUCTION

To describe neutron-rich matter which eventually appears in dense stellar objects, knowledge on the isospin part of the equation of state (EoS) is indispensable. Luckily, the isospin dependence of the EoS correlates strongly with the distribution of neutrons in nuclei; see [1–3] and references therein. Thus the thickness of neutron skins in nuclei impacts our knowledge of the structure of neutron stars [4–11]. Furthermore, the evolution of the neutron skin and proton distributions along isotope chains provide important information for our understanding of the nuclear structure over the whole nuclear chart [12–18].

The neutron skin thickness, ΔR_{np}, is usually defined as the difference between the root-mean-squared (rms) point radii of the neutron and proton density distributions. However, this definition is not unique because of possibly significant density variations both in the nuclear periphery and in the center [19] (see the discussion in Sec. V). Since quantal shell effects also influence the nucleon distributions, studies often focus on neutron-rich doubly magic nuclei, such as ^{40}Ca, ^{48}Ca, and ^{208}Pb.

Experimentally, charge distributions, which mainly reflect the proton distribution, can be explored rather precisely by electromagnetic probes such as electrons or muons. On the other hand, accurate information on neutron radii and neutron skins is scarce. Experimental techniques to determine the neutron distributions of nuclei using strongly interacting probes include proton elastic [20–24] and inelastic [25,26] reactions, measurement of interaction cross sections of heavy nuclei [12,17,20,27–29], and antiproton interactions [30]. The electric dipole response can be studied by α particle scattering exciting the giant dipole resonance [31,32], the excitation of the pigmy dipole resonance [33] and spin-dipole resonance [32,34], the electric dipole polarizability [35,36], pion scattering [15], coherent pion photoproduction [37], and antiprotonic x-rays [16,38]. The parity-violating electron scattering asymmetry provides a measure of the weak charge distribution and hence of neutron distribution in appropriate nuclei [39]. Finally, since neutron star properties and the neutron skins of nuclei are highly related [3], also astrophysical observations of neutron stars provide in an indirect way constraints on the neutron skin of, e.g., ^{208}Pb [40–42]. Despite these many experimental opportunities, the neutron distributions still carry considerable systematic uncertainties; see, for instance the discussions in Refs. [8,32,43].

Calcium isotopes are of particular value, since for such medium heavy nuclei already accurate *ab initio* calculations are possible [44–46], although in many cases a quantitative reproduction of nuclear radii is still an open issue [47,48]. Calculations using a wide variety of EoSs show a remarkable correlation between the slope parameter of the symmetry
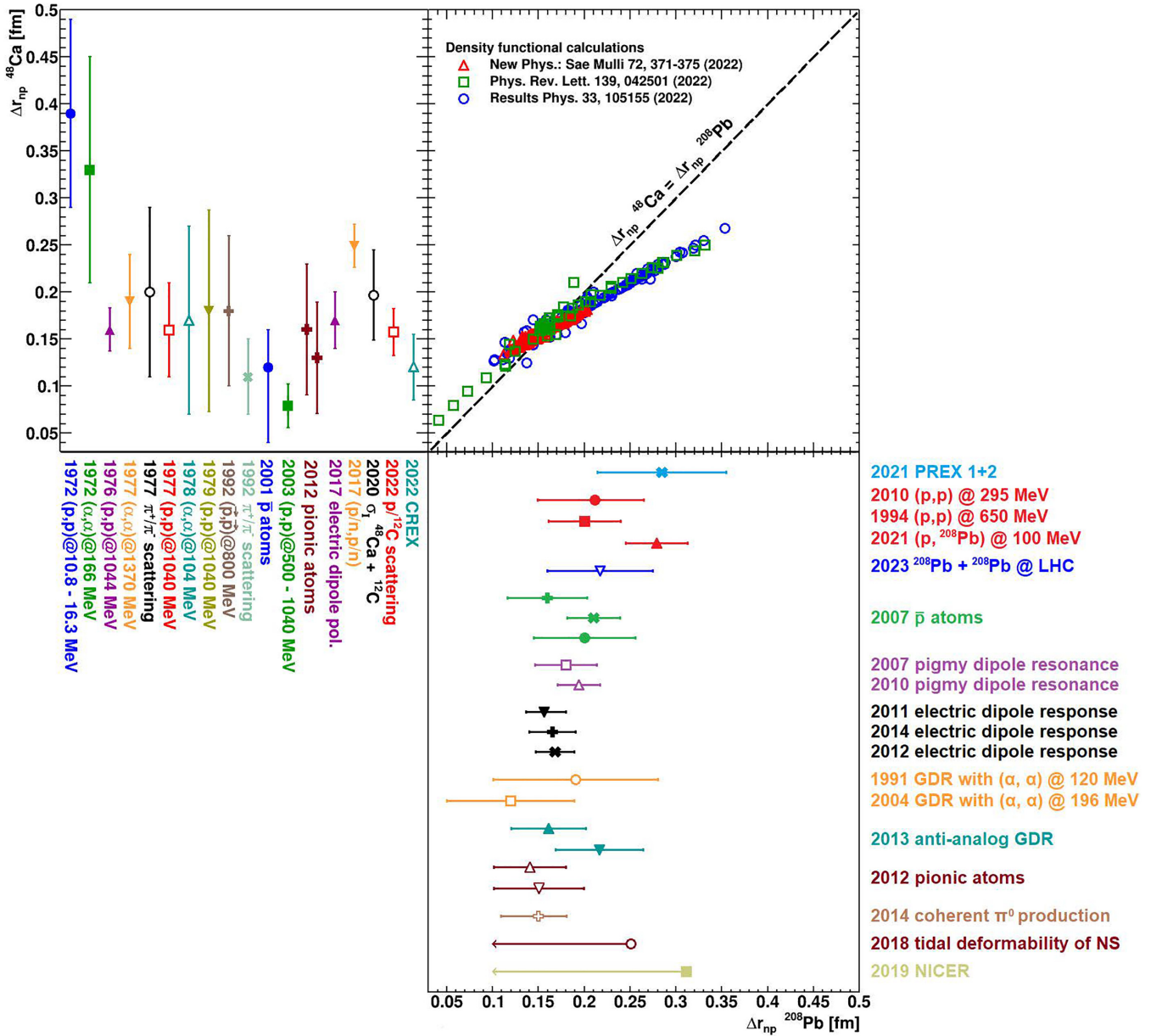
*Contact author: pochodza@uni-mainz.de

FIG. 1. Experimental values for the neutron skin thickness of the doubly magic nuclei ^{48}Ca (left panel) and ^{208}Pb (lower right panel). Detailed information on the displayed data are listed in Tables III and IV. The upper right panel shows the relation between the neutron skin thickness of ^{48}Ca or ^{208}Pb predicted by various models with different EoSs [20,39,49]. Note that the combined PREX measurement of ^{208}Pb [50,51] and the CREX result for ^{48}Ca [52] are in tension with these model predictions. References are listed in the Appendix.

energy and the neutron skin thickness of ^{48}Ca or ^{208}Pb. As consequence there exists a rather model independent correlation between the neutron skin thickness of these two nuclei [20,39,49] (see also in the upper right panel of Fig. 1). Data available for the two doubly magic nuclei ^{48}Ca and ^{208}Pb are exemplified in the left and lower panels in Fig. 1, respectively. Many of these analyses have sizable systematic uncertainties since the analyses are model dependent (for a recent analysis see, e.g., [53,54]). In this figure, statistical and systematic uncertainties (if available) were added in quadrature. Detailed information on the displayed data is provided in Tables III and IV in the Appendix.

A rather clean measure of the neutron distribution with small systematic uncertainties is expected from the electroweak asymmetry in elastic electron-nucleus scattering [39]. However, the PREX measurement of ^{208}Pb [50,51] and the CREX result for ^{48}Ca [52] are in tension with the expected correlation between the neutron skins of ^{48}Ca and ^{208}Pb shown in the upper right panel of Fig. 1. Indeed, for example, a recent nonlocal dispersive optical model analysis suggests a neutron skin for ^{208}Pb of $0.18^{+0.07}_{-0.06}$ fm [54], which is significantly lower than the PREX value, and for ^{48}Ca a skin of $0.22^{+0.02}_{-0.03}$ fm, which in turn is significantly larger than the
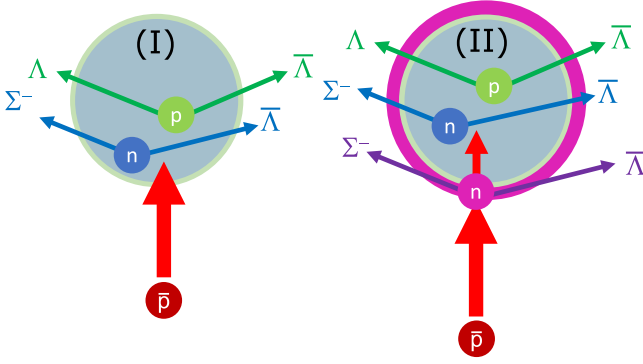
FIG. 2. Illustration of the production of $\Lambda\overline{\Lambda}$ and $\Sigma^-\overline{\Lambda}$ pairs in antiproton-nucleus interactions. We consider two isotopes (I) and (II) which differ by an additional outer neutron layer with thickness Δ_n, shown in pink. The production yields for the two different hyperon-antihyperon pairs provide a measurement of the effective thickness of this additional neutron layer.

CREX result. This situation clearly calls for further detailed theoretical [55] as well as improved experimental studies.

Throughout this work we present a novel method to explore the variation of the neutron skin between two different isotopes of a given element with high precision and accuracy. For that purpose we consider antiproton-nucleus interactions close to the thresholds of $\Lambda\overline{\Lambda}$ and $\Sigma^-\overline{\Lambda}$ pair production. At low energies, $\Lambda\overline{\Lambda}$ pairs are produced in $\overline{p} + p$ collisions, while $\Sigma^-\overline{\Lambda}$ pairs can only be produced in $\overline{p} + n$ interactions. Unlike other probes, antiprotons are strongly absorbed in the nuclear periphery and, therefore, are particularly sensitive to small variations of the nuclear skin.

Measuring the probabilities $p_{\Lambda\overline{\Lambda}}$ and $p_{\Sigma^-\overline{\Lambda}}$ for the two processes for a reference isotope (I) and a second isotope (II) allows one to determine the double ratio

$$\text{DR} = \frac{p^{\text{II}}_{\Sigma^-\overline{\Lambda}} \big/ p^{\text{II}}_{\Lambda\overline{\Lambda}}}{p^{\text{I}}_{\Sigma^-\overline{\Lambda}} \big/ p^{\text{I}}_{\Lambda\overline{\Lambda}}}. \tag{1}$$

Such a double ratio does not require the absolute determination of cross sections, and also the different energy dependence for the $\Lambda\overline{\Lambda}$ and $\Sigma^-\overline{\Lambda}$ channels is eliminated. Furthermore, measuring both production probabilities for a given isotope simultaneously, many experimental uncertainties cancel or can be significantly reduced.

Within a simple geometrical picture for central collisions, we first show in Sec. II that this ratio is strongly related to the difference of the neutron skin thicknesses of the two considered isotopes (I) and (II) depicted in Fig. 2.

In Sec. III we present a schematic scenario to describe the full impact parameter range. In Sec. IV, we compare these calculations with predictions of the Gießen Boltzmann-Uehling-Uhlenbeck (GiBUU) transport model [56] for various isotope pairs. Using the neutron distributions which describe the initial state in these GiBUU simulations, we find a remarkable correlation between the double ratio predicted by the simple picture of Sec. III and the double ratio predicted by the complete GiBUU simulations. As a consequence, the

simple scenario presented in Sec. III enables us to explore in Sec. V the sensitivity of the double ratio to variations of the neutron distributions. As a possible application at the $\overline{P}$ANDA experiment, we perform a systematic study for the case of ^{40}Ca and ^{48}Ca.

II. MOTIVATION OF THE METHOD: A SIMPLE SCENARIO

Because of the strong absorption of antiprotons in nuclei, the production of hyperon-antihyperon pairs happens in the nuclear periphery. For simplicity we consider a nearly central antiproton-nucleus collision (see left part of Fig. 2). Close to threshold, the probability $p^{\text{I}}_{\Lambda\overline{\Lambda}}$ to produce a $\Lambda\overline{\Lambda}$ pair within the reference nucleus (I) can be written as

$$p^{\text{I}}_{\Lambda\overline{\Lambda}} = \kappa_{\Lambda\overline{\Lambda}} \frac{\rho(p)}{\rho(p) + \rho(n)} \frac{\sigma_{\Lambda\overline{\Lambda}}}{\sigma_{\text{tot}}}. \tag{2}$$

Here σ_{tot} denotes the total $\overline{p} + A$ cross section and $\sigma_{\Lambda\overline{\Lambda}}$ is the elementary $\overline{p} + p \to \Lambda\overline{\Lambda}$ cross section. $\rho(p)$ and $\rho(n)$ denote the densities in the periphery of the target nucleus of protons and neutrons, respectively.

The factor $\kappa_{\Lambda\overline{\Lambda}}$ describes the loss of $\Lambda\overline{\Lambda}$ pairs due to absorptive rescattering. Similarly, the production probability of $\Sigma^-\overline{\Lambda}$ pairs can be approximated by

$$p^{\text{I}}_{\Sigma^-\overline{\Lambda}} = \kappa_{\Sigma^-\overline{\Lambda}} \frac{\rho(n)}{\rho(p) + \rho(n)} \frac{\sigma_{\Sigma^-\overline{\Lambda}}}{\sigma_{\text{tot}}}. \tag{3}$$

Because of the large annihilation cross section of antibaryons in nuclei, both $\kappa_{\Lambda\overline{\Lambda}}$ and $\kappa_{\Sigma^-\overline{\Lambda}}$ are dominated by the $\overline{\Lambda}$ absorption. Therefore, we assume $\kappa_{\Lambda\overline{\Lambda}} \approx \kappa_{\Sigma^-\overline{\Lambda}} \equiv \kappa_{\text{I}}$.

We now turn to an isotope (II) with a larger neutron number and hence a more extended neutron distribution. For simplicity, we assume that the proton distribution remains identical to the one of nucleus (I) and that the neutron distribution is only extended by an additional skin Δ_n at the surface; see the pink area in the right part of Fig. 2. Such a situation, approximately, is found in isotope chains of heavy nuclei. In such a scenario, the production of $\Lambda\overline{\Lambda}$ pairs is reduced by the absorption probability p_{abs} of the incident antiprotons within this additional neutron skin Δ_n:

$$p^{\text{II}}_{\Lambda\overline{\Lambda}} = (1 - p_{\text{abs}})\kappa_{\text{II}} \frac{\rho(p)}{\rho(p) + \rho(n)} \frac{\sigma_{\Lambda\overline{\Lambda}}}{\sigma_{\text{tot}}}. \tag{4}$$

The absorption probability p_{abs} can be expressed in terms of the total $\overline{p} + n$ reaction cross section $\sigma_{\overline{p}n}$ [57] and the integrated skin density $\int_{\Delta_n} \rho_n \, dr_n$ of the additional neutron skin of nucleus (II) with respect to the reference nucleus (I):

$$1 - p_{\text{abs}} \approx \exp\left\{ -\sigma_{\overline{p}n} \int_{\Delta_n} \rho_n dr_n \right\}. \tag{5}$$

Like the incoming antiprotons, the produced $\overline{\Lambda}$ are also absorbed in the additional neutron layer. We use the factorization ansatz $\kappa_{\text{II}} = \kappa_{\text{I}}\kappa_n$. With this simplification, we can express Eq. (4) as

$$p^{\text{II}}_{\Lambda\overline{\Lambda}} = \kappa_n(1 - p_{\text{abs}})p^{\text{I}}_{\Lambda\overline{\Lambda}}. \tag{6}$$

The production of $\Sigma^-\overline{\Lambda}$ pairs gains an additional component from the additional neutron skin. On the other hand, the

contribution from the inner part of the nucleus (II) is reduced by the loss of antiprotons in the additional neutron layer:

$$p_{\Sigma^-\overline{\Lambda}}^{\mathrm{II}} = \kappa_{\mathrm{II}} p_{\mathrm{abs}} \frac{\sigma_{\Sigma^-\overline{\Lambda}}}{\sigma_{\mathrm{tot}}}$$

$$+ (1 - p_{\mathrm{abs}}) \kappa_{\mathrm{II}} \frac{\rho(n)}{\rho(p) + \rho(n)} \frac{\sigma_{\Sigma^-\overline{\Lambda}}}{\sigma_{\mathrm{tot}}}. \quad (7)$$

Here, we assume that the loss of outgoing Σ^- and/or $\overline{\Lambda}$ for pairs produced in the additional neutron skin is the same as for pairs produced within the core nucleus. We thus obtain for the double ratio

$$\mathrm{DR} = \frac{p_{\Sigma^-\overline{\Lambda}}^{\mathrm{II}} \big/ p_{\Lambda\overline{\Lambda}}^{\mathrm{II}}}{p_{\Sigma^-\overline{\Lambda}}^{\mathrm{I}} \big/ p_{\Lambda\overline{\Lambda}}^{\mathrm{I}}} = \frac{p_{\mathrm{abs}} \frac{\rho(p)+\rho(n)}{\rho(n)} + (1 - p_{\mathrm{abs}})}{1 - p_{\mathrm{abs}}}. \quad (8)$$

With the simplifying assumption $\rho(p) = \frac{Z}{N}\rho(n)$, where Z denotes the element number and N the neutron number of the reference isotope I, we finally find for the double ratio the expression

$$\mathrm{DR} = \frac{1 + p_{\mathrm{abs}} Z/N}{1 - p_{\mathrm{abs}}} \quad (9)$$

Since the variation of the neutron skin thickness is rather small, the additional absorption probability p_{abs} is also small. In this case, we can expand Eq. (9) and obtain a linear relation between the double ratio DR and the absorption probability of the incident antiprotons within the increased neutron skin Δ_n:

$$\mathrm{DR} \approx 1 + \left(1 + \frac{Z}{N}\right) p_{\mathrm{abs}}. \quad (10)$$

This expression is nearly independent of the considered nuclei, and it signals that DR is a direct measure of the increment of (integrated) neutron skin thickness. The only quantity to be known is the total $\overline{p} + n$ reaction cross section $\sigma_{\overline{p}n}$, which can be determined from experiment by comparing, e.g., $\overline{p}p$ and $\overline{p}d$ interactions.

III. FINITE IMPACT PARAMETER RANGE

Of course, this simplified geometrical picture has several deficiencies:

(i) In $\overline{p}$-A collisions one cannot constrain the impact parameter and one, therefore, has to consider the full impact parameter range.

(ii) The diffuseness of the neutron periphery and possible differences between two isotopes are neglected.

(iii) Usually incident antiprotons do not traverse the skin radially and the absorption probability depends on the impact parameter.

(iv) The absorption of produced antihyperons favor the pair production in peripheral reactions.

(v) Different isotopes may also have different proton distributions.

Because of the large absorption cross section for antiprotons, the production ratio for $\Sigma^-\overline{\Lambda}$ and $\Lambda\overline{\Lambda}$ pairs reflects the neutron and proton content of the nuclear periphery and will,
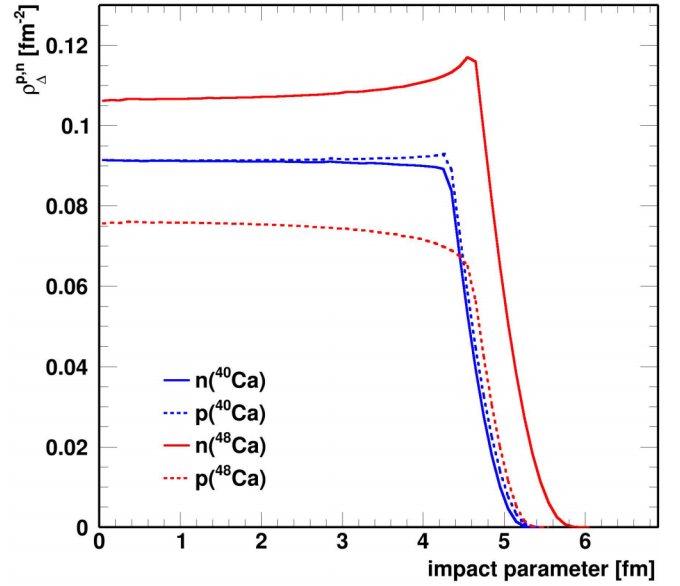

FIG. 3. Individual areal densities for protons (dashed lines) and neutrons (solid lines) within one interaction length for ^{40}Ca (blue lines) and ^{48}Ca (red lines) at an incident momentum of 2.4 GeV/c according to Sec. III. The density distributions were generated during the initialization of the Gießen Boltzmann-Uehling-Uhlenbeck (GiBUU) transport model simulations [56] using the RMF parameter set of Ref. [58].

therefore, be strongly related to the neutron neutron skin or halo. However, one has to keep in mind that particularly at low beam energies the production ratio of $\Sigma^-\overline{\Lambda}$ and $\Lambda\overline{\Lambda}$ pairs is influenced by different production cross sections. Considering the double ratio for two isotopes, this dependence largely cancels. In the following, we will calculate the production ratio between $\Sigma^-\overline{\Lambda}$ and $\Lambda\overline{\Lambda}$ pairs for two isotopes [see Eq. (1)] by evaluating the double ratio of the component areal densities for neutrons and protons within one attenuation length for the two considered isotopes.

In this work we consider an incident $\overline{p}$ momentum of 2.4 GeV/c. At this energy, the interaction cross sections of $\overline{p} + p$ and $\overline{p} + n$ are similar in magnitude and are about 55 mb [57]. For such a cross section, the interaction length at normal nuclear density of 0.16 fm^{-3} is about $\Delta = 1.14$ fm, corresponding to an integrated areal density along the antiproton path of $\int_\Delta \rho_{n+p}\,\mathrm{d}z \approx 0.18$ fm^{-2}. In the periphery, where the density is low, this integral is of course limited by the lower total areal density.

The density distributions used in the following are generated during the initialization of the GiBUU simulations using the RMF parameter set of Ref. [58]. Assuming for simplicity a straight line trajectory along the z direction for the incident antiproton, Fig. 3 shows the areal density $\rho_\Delta^q(b) = \int_\Delta \rho_q dz$ for protons ($q = p$; red lines) and neutrons ($q = n$; blue lines) along the antiproton path within one interaction length Δ for ^{40}Ca (dashed lines) and ^{48}Ca (solid lines) as a function of the impact parameter b. Of course, at large impact parameters, where the nuclear density is low, a full interaction length can not be reached and the integrated areal densities

TABLE I. Isotopes studied in this work. The second and third column give the natural abundances and the experimental charge radii. Proton and neutron rms radii and their differences predicted by the relativistic mean field model of Ref. [58] for stable or long-lived isotopes are listed in columns 4 to 7. The radial distributions are generated during the initialization of the Gießen Boltzmann-Uehling-Uhlenbeck (GiBUU) transport model simulations [56].

Isotope	Abundance (%)	Expt. charge radius R_p^{exp} (fm)	Proton radius R_p (fm)	Neutron radius R_n (fm)	Neutron skin ΔR_{pn} (fm)	Skin difference Δ_n (fm)	RMF model
^{20}Ne	90.5	2.992 ± 0.008 [59]	2.782	2.758	-0.024		NL3 [58]
^{22}Ne	9.3	2.986 ± 0.021 [59]	2.800	2.887	0.087	0.111	NL3 [58]
^{40}Ca	96.9	3.4776 ± 0.0019 [60]	3.452	3.416	-0.036		NL1 [58]
^{48}Ca	0.187	3.4786 ± 0.0106 [60,61]	3.525	3.731	0.206	0.242	NL1 [58]
^{40}Ca	96.9	3.4776 ± 0.0019 [60]	3.391	3.354	-0.037		NL3 [58]
^{48}Ca	0.187	3.4786 ± 0.0106 [60,61]	3.472	3.659	0.187	0224	NL3 [58]
^{40}Ca	96.9	3.4776 ± 0.0019 [60]	3.396	3.360	-0.036		NL3* [62]
^{48}Ca	0.187	3.4786 ± 0.0106 [60,61]	3.475	3.666	0.191	0.227	NL3* [62]
^{58}Ni	68.1	3.770 ± 0.002 [63]	3.769	3.768	0.000		NL3 [58]
^{64}Ni	0.926	3.854 ± 0.002 [63]	3.822	3.947	0.125	0.125	NL3 [58]
^{129}Xe	26.4	4.7775 ± 0.0050 [60]	4.768	4.932	0.164		NL3 [58]
^{130}Xe	4.1	4.7818 ± 0.0049 [60]	4.776	4.950	0.174	0.010	NL3 [58]
^{131}Xe	21.2	4.7808 ± 0.0049 [60]	4.784	4.968	0.184	0.020	NL3 [58]
^{132}Xe	26.9	4.7859 ± 0.0048 [60]	4.792	4.986	0.194	0.030	NL3 [58]
^{134}Xe	10.4	4.7899 ± 0.0047 [60]	4.809	5.023	0.213	0.049	NL3 [58]
^{136}Xe	8.9	4.7964 ± 0.0047 [60]	4.826	5.059	0.233	0.069	NL3 [58]

are lower. Whereas for ^{40}Ca the proton and neutron content within Δ is rather similar, for ^{48}Ca the neutrons exceed the protons by more than 50%. Integrating the individual components for protons ($q = p$) or neutrons ($q = n$) over all impact parameters,

$$P^q = \frac{\int_{b=0}^{\infty} \rho_\Delta^q(b)\, b\, db}{\int_{b=0}^{\infty} b\, db}, \qquad (11)$$

we find a neutron-to-proton ratios $P^n/P^p = 0.97$ and 1.65 for ^{40}Ca and ^{48}Ca, respectively. The expected double ratio amounts then to $1.65/0.97 \approx 1.70$. The last column in Table II lists the double ratios expected for all studied isotope pairs and different RMF parameters from this schematic scenario. To illustrate the sensitivity of the method in the case of only small variations of the neutron distribution, we explore here first the isotope chain of xenon. At an antiproton storage ring, xenon can be experimentally explored in the mass range from $A = 129$ to $A = 136$. Of course, one has to keep in mind that an efficient gas recirculation system will be mandatory. The filled red squares and blue points in Fig. 4 show the rms radii of the proton and neutron distributions as a function of the Xe mass number. In these calculations not only the neutron radii but, unlike in the simple geometrical picture presented above, also the proton radii are rising slightly with increasing neutron number. This increasing charge radius is qualitatively consistent with experimental data—see open squares in Fig. 4 [60]—though the experimental slope with the mass number is only about half as large. Note that the range of the neutron skin varies by only 0.13 fm, which is only a factor of 2 larger than the uncertainty of the PREX measurement for Pb. Since parity violating e^- scattering is generally hampered by limited statistics, exploring such small neutron skin

variation in heavy isotope chains clearly calls for alternative methods.

Figure 5 shows the double ratio from the two simplified scenarios in Sec. II (blue squares) and Sec. III (green dots) for xenon isotopes with mass $A = 130$–136 with respect to ^{129}Xe. Compared to the simple analytic expression of Eq. (9) with
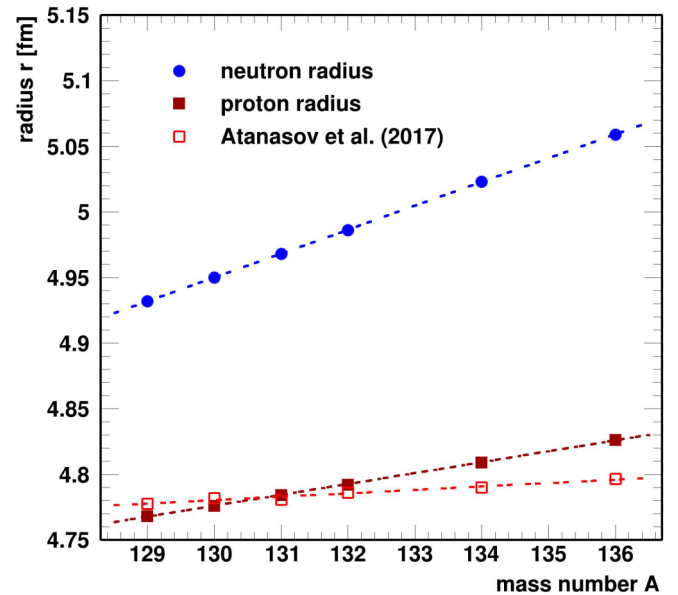

FIG. 4. Proton (filled red squares) and neutron (blue points) rms radii of the initial distributions for stable or long-lived xenon isotopes used by the GiBUU simulations [56]. The open red squares show experimental values for the proton radii [60,64]. The lines are drawn to guide the eye.

TABLE II. Number of generated inclusive interactions and production yield of $\Lambda\overline{\Lambda}$ and $\Sigma^-\overline{\Lambda}$ pairs in $\overline{p}$-Ne, -Ca, -Ni, and -Xe interactions at an incident momentum of 2.4 GeV/c. The last three columns show the double ratios deduced from the GiBUU simulation [56], and the simple models presented in Secs. II and III.

Target	RMF model	Events ($\times 10^6$)	Number of pairs		Double ratio		
			$\Lambda\overline{\Lambda}$	$\Sigma^-\overline{\Lambda}$	GiBUU	Eq. (9)	ρ_Δ (Sec. III)
^{20}Ne	NL3 [58]	167	32387	10870			
^{22}Ne	NL3 [58]	171	29227	13297	1.356 ± 0.021	1.100	1.291
^{40}Ca	NL1 [58]	415	76323	22880			
^{48}Ca	NL1 [58]	450	66694	36074	1.799 ± 0.018	1.225	1.683
^{40}Ca	NL3 [58]	415	74280	21827			
^{48}Ca	NL3 [58]	450	61313	32391	1.798 ± 0.019	1.207	1.683
^{40}Ca	NL3* [62]	415	78753	23438			
^{48}Ca	NL3* [62]	450	64212	34523	1.807 ± 0.018	1.210	1.685
^{58}Ni	NL3 [58]	100	16811	5230			
^{64}Ni	NL3 [58]	108	14978	6534	1.402 ± 0.030	1.109	1.340
^{129}Xe	NL3 [58]	109	13717	6238			
^{130}Xe	NL3 [58]	109	13394	6225	1.022 ± 0.022	1.008	1.023
^{131}Xe	NL3 [58]	109	13403	6379	1.047 ± 0.023	1.015	1.047
^{132}Xe	NL3 [58]	109	13335	6556	1.081 ± 0.023	1.023	1.071
^{134}Xe	NL3 [58]	109	12771	6656	1.146 ± 0.025	1.037	1.120
^{136}Xe	NL3 [58]	109	12680	6739	1.169 ± 0.025	1.053	1.170

zero impact parameter, the ratio is significantly enhanced by considering the full impact parameter range. This is caused by the larger role played by the neutron-rich nuclear periphery at large impact parameters. Within this picture a significant
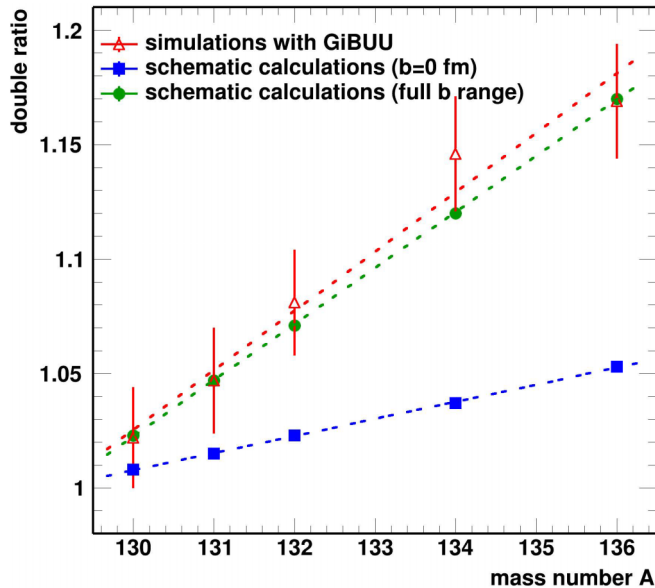

FIG. 5. Double ratio predicted from the two simplified scenarios in Sec. II (blue squares) and Sec. III (green dots) for different xenon isotopes of mass $A = 130$–136 with respect to ^{129}Xe. The density distributions were generated during the initialization of the Gießen Boltzmann-Uehling-Uhlenbeck (GiBUU) transport model simulations [56] using the RMF parameter set of Ref. [58]. The red triangle show the results of the GiBUU simulations. The lines are drawn to guide the eye.
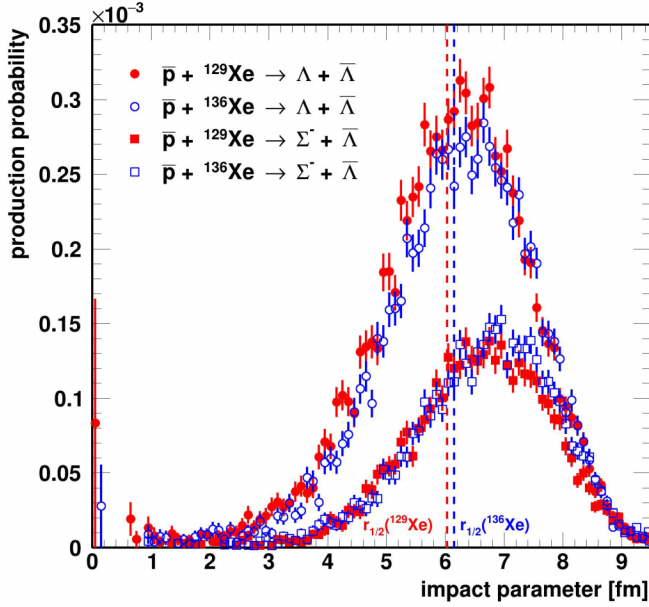
variation of the double ratio over such an isotope chain is expected.

IV. GIBUU TRANSPORT STUDY

A more realistic description of the hyperon pair production can be achieved by microscopic transport calculations. One such model, the Gießen Boltzmann-Uehling-Uhlenbeck (GiBUU) transport model [56], describes many features of $\overline{p}$-nucleus interactions in the FAIR (Facility for Antiproton and Ion Research) energy range [56,65,66]. Particularly the presently available data on strangeness production are well reproduced. These simulations also avoid the approximations adopted in the derivation of Eq. (9). In future studies we will also consider the coplanarity of the produced hyperon-antihyperon pair to extract additional information. However, in the present work we restrict the discussion to the total production ratios.

In the following, we employ the GiBUU model to study $\overline{p}$ + Ne, Ca, Ni, and Xe reactions of several isotopes. All studied isotopes have a sizable abundance (Table I) and can in principle be used for experimental studies. The simulations were performed with an incident antiproton momentum of 2.4 GeV/c.

The number of generated events for each nucleus are listed in Table II. Typically, 100 million events require a computational time of about four days on the MOGON2 high performance computing cluster at the University of Mainz. During the initialization of these simulations, the proton and neutron distributions of the target nuclei are generated by a self-consistent relativistic mean-field (RMF) model. If not mentioned otherwise, we use the RMF parameter set of Ref. [58].

FIG. 6. Production probability of $\Lambda\overline{\Lambda}$ pairs (circles) and $\Sigma^-\overline{\Lambda}$ pairs (squares) predicted by the GiBUU transport model [56] in exclusive 2.4 GeV/c $\overline{p}$-^{129}Xe (red symbols) and $\overline{p}$-^{136}Xe (blue symbols) interactions as a function of the impact parameter. For orientation, the two lines mark the half-density radii $r_{1/2}$ of ^{129}Xe (red line) and ^{136}Xe (blue line).

A. The case of xenon isotope chain

Figure 6 shows the predicted production probability $\sim b^{-1} dN_{Y\overline{\Lambda}}/db$ for $\Lambda\overline{\Lambda}$ pairs (circles) and $\Sigma^-\overline{\Lambda}$ pairs (squares) as a function of the impact parameter b for for ^{129}Xe (red) and ^{136}Xe (blue) interactions. The vertical dashed lines indicate rms radii for neutrons and protons of ^{129}Xe (red) and ^{136}Xe (blue; see Table I). As expected, the pair production probability is largest in the nuclear periphery, where the chance of both the $\overline{\Lambda}$ and the Λ or Σ^- escaping is sizable. At very small impact parameters, particularly the forward going $\overline{\Lambda}$ have to cross a large part of the target nucleus to be emitted. Consequently, for heavy nuclei like xenon the absorption probability for $\overline{\Lambda}$ approaches 1 for more central collisions.

Figure 7 shows the ratio of exclusive $\Lambda\overline{\Lambda}$ (red symbols) and $\Sigma^-\overline{\Lambda}$ pair production in ^{136}Xe vs ^{129}Xe nuclei as a function of the impact parameter. At impact parameters around the nuclear radius, the $\Lambda\overline{\Lambda}$ production in $\overline{p} + p$ interactions is reduced for the more neutron-rich isotope due to the more extended neutron skin, which leads to an enhanced absorption for the incoming $\overline{p}$ as well as the outgoing $\overline{\Lambda}$. At very large impact parameters beyond >7 fm, and at hence low matter density, the antiprotons are hardly absorbed and the antiprotons surpass the full proton (and neutron) distributions. Since the proton distributions are quite similar for the two isotopes, the $\Lambda\overline{\Lambda}$ ratio approaches 1.

The production ratio for $\Sigma^-\overline{\Lambda}$ pairs indicated by blue symbols in Fig. 7 shows a somewhat different impact parameter dependence. For $\Sigma^-\overline{\Lambda}$ production, the absorptions of the incident antiprotons and the produced $\overline{\Lambda}$ within an extended
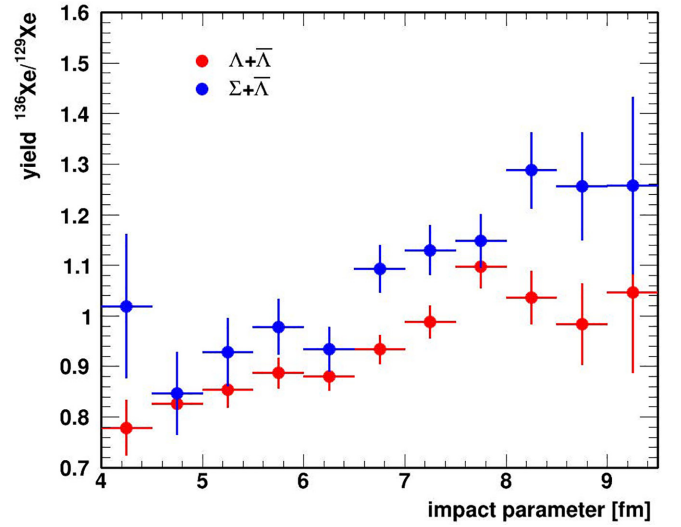

FIG. 7. Ratio of exclusive $\Lambda\overline{\Lambda}$ (red) and $\Sigma^-\overline{\Lambda}$ pair production in ^{136}Xe vs ^{129}Xe nuclei as a function of the impact parameter.

neutron skin act in opposite directions. Indeed, a weak suppression is observed at more central collisions and the region of intermediate impact parameters shows similar yields for ^{129}Xe and ^{136}Xe. However, going further into the low density periphery of the nuclei beyond $b > 6$ fm, the absorption of the $\overline{\Lambda}$ is less important and the additional neutron content of ^{136}Xe enhances the $\Sigma^-\overline{\Lambda}$ production with respect to ^{129}Xe considerably.

Table II gives the individual yields for all six isotopes and the yield ratios between $^{130-136}$Xe and ^{129}Xe. Already the individual yields show a continuous sensitivity to the additional neutron layer in ^{136}Xe. Since the yield ratios R for $\Lambda\overline{\Lambda}$ and $\Sigma^-\overline{\Lambda}$ pairs are affected in opposite directions, the sensitivity is even more enhanced by forming the double ratio DR of Eq. (1). Despite the small neutron skin variations between ^{129}Xe and ^{136}Xe of only 0.07 fm (see Table I), the skin variation correlates strongly with the double ratio calculated with the GiBUU code with a Pearson correlation of 0.984 for these xenon data.

It is interesting to note that the double ratio from the GiBUU simulations (red triangles in Fig. 5) and the ratios from our simplified calculations of Sec. III (green dots in Fig. 5) agree within errors. Although the quantitative agreement may be fortuitous, this strong correlation shows that the simple analytic model outlined in Sec. III covers the main features of the process. This will be discussed in more detail at the end of this section and in Sec. V.

B. The case of ^{20}Ne and ^{22}Ne

Like the noble gas xenon, neon is also a feasible element for the $\overline{P}$ANDA cluster-jet target. Besides the common isotope ^{20}Ne, also ^{22}Ne might be a feasible target if the cluster target system is equipped with a gas regeneration system. The measured charge radii of ^{20}Ne ($r_c = 2.992 \pm 0.008$ fm) and ^{22}Ne ($r_c = 2.986 \pm 0.021$ fm) differ very little [59]. This small variation is also reproduced by Hatree-Fock-Bogoliubov [67]

and relativistic mean field calculations [68]. On the other hand, according to these calculations, the radius of the neutron distribution of ^{22}Ne is about 0.2 fm wider than the one of ^{20}Ne [67]. The RMF model implemented in the GiBUU code gives a difference which is about half as large (see Table I).

The upper part of Table II gives the individual yields and the yield ratios for ^{22}Ne and ^{20}Ne targets predicted by GiBUU for an incident antiproton momentum of 2.4 GeV/c. Unlike for the xenon isotopes, already the individual yields show a remarkable sensitivity to the additional neutron layer in ^{22}Ne. Since the yield ratios for $\Lambda\overline{\Lambda}$ and $\Sigma^-\overline{\Lambda}$ pairs are affected in opposite directions by the additional neutron layer, the sensitivity is even more enhanced by forming the double ratio DR, which reaches a value around 1.4.

C. The case of ^{40}Ca and ^{48}Ca

Charge radii of calcium isotopes are very well known [69]. Indeed, ^{48}Ca has the same rms charge radius as ^{40}Ca within 0.001 ± 0.003(stat.) ± 0.010(syst.) fm [61], making this isotope pair an ideal case for the proposed method. One has to keep in mind though that the proton density *distributions* also show significant differences [70,71].

The GiBUU model evaluates the initial charge and neutron distributions of the target nucleus with a specified RMF parameter set. The same parametrization also enters during the time evolution of the reaction. Of course, any interpretation of experimental data should be constrained to simulations that describe the proton distributions (and other possible observables) reasonably well. In the present work we use three RMF descriptions, NL1 [58], NL3, and NL3* [62], which provide slightly different proton and neutron distributions. In all three cases the proton radii are close to the experimental values (see Table I). In line with the similar proton and neutron distributions, the double ratios from the GiBUU simulations agree within statistical uncertainties for all three cases (see Table II).

In Fig. 8 we depict the double ratio deduced from the neutron-proton content of the nuclear periphery as described in Sec. III as a function of the double ratio predicted by the GiBUU transport calculations of 2.4 GeV/c $\overline{p}+A$ interactions. The systematic difference between the two double ratios can be, at least in part, traced back to the difference in absorption of antihyperons and hyperons, which is particularly large at small impact parameters, where the double ratio is smaller (cf. Figs. 7 and 3). In our schematic model this absorption effect has been neglected. Nonetheless, the strong correlation between the two quantities in Fig. 8 with a slope close to 0.9 and with a remarkable Pearson coefficient of 0.999 suggests that our schematic model accounts for the main features of the reaction process modeled by the GiBUU code. The fact that this linear correlation holds over a wide mass and element range is also in line with Eq. (10), which itself indicates within the (oversimplified) scenario of Sec. II the dominance of the neutron skin difference. It seems that the double ratio is not strongly influenced by the dynamics of the reaction process.

In cases where predictions for the density distributions of protons and neutrons exist, the prescription of Sec. III and the
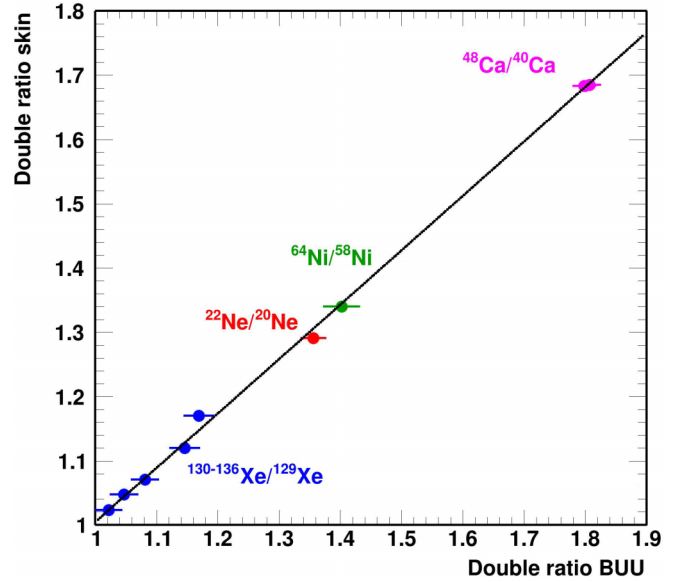

FIG. 8. Double ratio deduced from the neutron-proton content of the nuclear periphery as described in Sec. III as a function of the double ratio predicted by the GiBUU transport calculations of 2.4 GeV/c $\overline{p}+A$ interactions. The black line is a linear fit to the data. The Pearson coefficient between the two double rations amounts to 0.999.

correlation of Fig. 8 allow the evaluation of the double ratio, which could be confronted with experiments.

V. SENSITIVITY AND SYSTEMATICS OF THE METHOD

A. General aspects

The results for the xenon isotopes give an important hint about the sensitivity of double ratios to the thickness of the neutron skin. It is, however, highly desirable to investigate that relation systematically on more general grounds. Under theoretical aspects, one may use results obtained by a representative selection of nuclear models. That was the approach pursued in the previous sections: The RMF models incorporated into the GiBUU numerical transport package are well tested and widely and successfully used mean-field models. The results are typical at least for covariant nonlinear energy density functionals. Since modern mean-field approaches lead within error bars to the same results for nuclear masses and form factors, the GiBUU-based result discussed in the previous sections can be considered to be valid and realistic even beyond the special class of built-in mean-field approaches. Obviously, extending the list to other covariant or noncovariant energy density functional approaches will not lead to fundamentally different conclusions.

However, it is still of value to dig a bit deeper into the relation between antiproton-nucleus double ratios and the nuclear skin properties. It is worthwhile to recall that the rms radius, together with the diffusivity, and the half-density radius, as defining key element of nuclear density distributions, are of high research interest. Most spectacularly, this is reflected by unexpected results of the PREX/CREX experiments on the

neutron skin in ^{208}Pb. They are in tension with the seemingly well established former, largely theoretically based knowledge on that issue.

In this paper and especially in this section we anticipate that antiproton annihilation on nuclei provides an independent approach to nuclear skin research. For that aim, we set aside for the moment the numerically involved self-consisted RMF description and revert to an easy-to-handle, but realistic, schematic approach. Except for the lightest nuclei, nuclear density distributions are well described by form factors of Wood-Saxon shape. Proton ($A_q = Z$) and neutron ($A_q = N \equiv A - Z$) number density distributions are parametrized by Fermi-distributions

$$\rho_q(r) = \frac{\rho_0(A_q)}{1 + e^{(r-R_q)/a_q}}, \qquad (12)$$

where for simplicity we assume spherical symmetry. The half-density radius R_q and diffuseness a_q may be adjusted to electron scattering data or to theoretical RMF or nonrelativistic HFB results, respectively. Normalization to the respective mass and charge numbers leads to

$$\rho_0(A_q) = \frac{3A_q}{4\pi R_q^3(1 + x_q)}, \qquad (13)$$

where $x_q = (\frac{\pi a_q}{R_q})^2$ and $\rho_0(A_q) \sim \rho_q(r)|_{r=0}$ is the density at the center of the nucleus. The mean-square radius is

$$\langle r_q^2 \rangle = \frac{3}{5}R_q^2 \left(\frac{1 + \frac{121}{30}x_q + \frac{7}{3}x_q^2}{1 + x_q} \right). \qquad (14)$$

The expressions of Eqs. (13) and (14) are correct up to terms of order $O(e^{-R_q/a_q})$. For $a_q = 0$ the expressions of Eqs. (13) and (14) reduce to the respective hard sphere results that we adopted in Sec. II. The two central messages of this exercise are first that the nuclear geometrical parameters are in fact intimately and nonlinearly correlated, and second that strict constraints on parameter variations are imposed by the requirement that the normalization to proton and neutron numbers must be maintained separately. A clear advantage of the Fermi-function model is to illustrate those aspects of nuclear density distributions in a very transparent manner.

In this section we concentrate on the isotope pair of ^{40}Ca and ^{48}Ca. To mimic the effect of different nuclear models, we modify the neutron distribution of ^{48}Ca. In the following, two nominally different scaling approaches will be used to study possible statistical and systematic uncertainties.

B. Radial scaling as a form-invariant transformation

The Fermi-function model is an ideal tool to clarify the connections between radial scaling and scaling of density parameters. Radial scaling by a factor α amounts to stretch ($\alpha > 1$) or squeeze ($0 < \alpha < 1$) the radial coordinate:

$$\rho_q(r) \to \widetilde{\rho}_q(\alpha r) \qquad (15)$$

constrained by

$$A_q = \int d^3r \rho_q(r) = \int d^3r_\alpha \widetilde{\rho}_q(r_\alpha), \qquad (16)$$
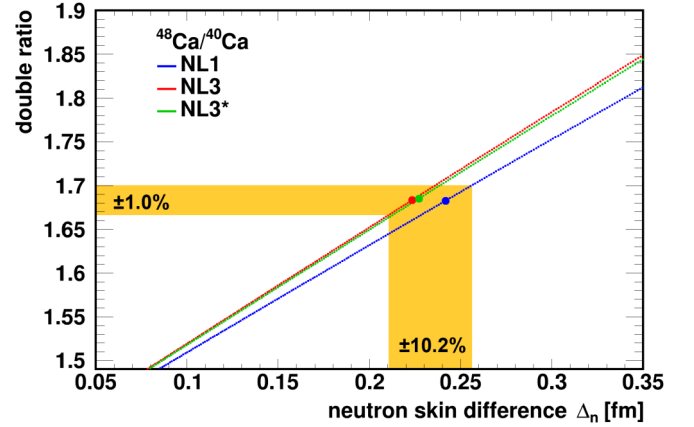

FIG. 9. Double ratio deduced from the neutron-proton content of the nuclear periphery versus the difference of the neutron skin thickness Δ_n for ^{40}Ca and ^{48}Ca. In order to explore the effect of different neutron skins for ^{48}Ca, its neutron distribution generated by GiBUU was artificially scaled in the radial direction by a given factor, while the proton distribution and the distributions for ^{40}Ca remained unchanged. The density distributions are generated during the initialization of the GiBUU simulations [56] using the RMF parameter set of Ref. [58].

which corresponds to requiring equality of the integrands, $d^3r\rho_q(r) = d^3r_\alpha \widetilde{\rho}_q(r_\alpha)$. The norm integral is conserved by using $\widetilde{\rho}_q(\alpha r) = \rho_q(\alpha r)$ and $d^3r_\alpha = \alpha^3 d^3r$, or alternatively, $\widetilde{\rho}_q(r_\alpha) = \alpha^3 \rho_q(\alpha r)$ combined with the unchanged volume element $d^3r_\alpha = d^3r$.

Modeling the nucleon density distributions by Fermi functions, radial scaling produces

$$\rho_q(\alpha r) = \frac{\rho_0(A_q)}{1 + e^{(\alpha r - R_q)/a_q}} = \frac{\rho_0(A_q)}{1 + e^{(r - R_q^{(\alpha)})/a_q^{(\alpha)}}} \qquad (17)$$

with $R_q^{(\alpha)} = R_q/\alpha$ and $a_q^{(\alpha)} = a_q/\alpha$. Hence, radial scaling corresponds to scaling simultaneously the half-density radius R_q and the diffusivity a_q by the same factor. Hence, we are led to the conclusion that radial scaling is a rather restrictive approach because mathematically it is a shape-invariant transformation. Still, it can be used to estimate statistical uncertainties of the method.

Of course, such a radial scaling can be applied to any distribution. For this study we make use of density distributions which are generated with the initialization code of the GiBUU simulations [56] using different RMF parameter sets of Ref. [58]. We consider here only parameter sets which give proton radii in good agreement with the experimental values (see Table I). First, the neutron density distribution of ^{48}Ca was radially scaled. Subsequently, the neutron density distribution was renormalized to the total number of neutrons of 28. As stressed before, the diffuseness of the neutron skin is scaled correspondingly. The neutron distribution of ^{40}Ca and the proton distributions of both isotopes remained unchanged.

Figure 9 shows the double ratio calculated as described in Sec. III versus the difference Δ_n of the neutron skin between the ^{40}Ca nucleus and the modified ^{48}Ca nucleus, $\Delta_n = \Delta R_{pn}(^{48}\text{Ca}) - \Delta R_{pn}(^{40}\text{Ca})$. The symbols on each line mark the double ratio and neutron skin difference for the original

density distributions (cf. Table I). For all three interaction parameters we find a very similar linear relation between the double ratio and Δ_n. An uncertainty of the double ratio of $\pm 1\%$, which is typical for the GiBUU data sets in this work (see Table II) translates into an uncertainty of the neutron skin variation by about $\pm 7\%$. Including possible systematic variations due to the three different interactions, an uncertainty of the double ratio of $\pm 1\%$ translates into an uncertainty of the neutron skin variation by about $\pm 10\%$ (see yellow bands in Fig. 9). This is about a factor of 3 smaller compared to the uncertainty of the CREX result.

C. Two-parameter scan in the Fermi model

If nuclear density distributions would obey radial scaling, then knowing one nuclear density would be sufficient for knowing the density distributions of all nuclei. Obviously, that is not the case. In reality, nuclear density distributions depend on the properties of the wave function, seen most impressively in neutron-rich halo nuclei. Thus, half-density radius and diffuseness evolve with proton and neutron number by their own rules, defined by the shell structure, i.e., single-particle angular momentum, and separation energies which are determined by the interplay of the various components of the nuclear mean field, including long-range Coulomb interactions.

The Fermi-function approach provides the degrees of freedom necessary for realistically modeling the nuclear density distribution. The general case is given by varying independently R_q and a_q:

$$\rho_q^{(\lambda,\kappa)} = \rho_0^{(\lambda,\kappa)}(A_q) \frac{1}{1 + e^{(r - R_q^{(\lambda)})/a_q^{(\kappa)}}}, \qquad (18)$$

where $\rho_0^{(\lambda,\kappa)}(A_q)$ is defined with the scaled parameters $R_q^{(\lambda)} = \lambda R_q$ and $a_q^{(\kappa)} = \kappa a_q$, assuring the proper normalization. Evidently, the above ansatz allows one to study shape variations, induced by changes in R_q and/or a_q.

As pointed out in our Introduction, the characterization of the neutron density distributions in terms of a single quantity like the root-mean-squared radius is a major simplification. In fact, differing nuclear density distributions may lead to the same rms radius. This can be nicely illustrated by the two-parameter Fermi distribution function, where the rms radius depends on both the radius and the diffuseness of the distribution [see Eq. (14)]. Requiring for example a fixed $R_{rms} = 4$ fm, a variation of the diffuseness parameter by $\Delta a_q = \pm 0.05$ fm can be compensated by a variation of $\Delta R_q \approx \mp 0.12$ fm and vice versa. For orientation, the diffuseness parameters of ^{40}Ca and ^{48}Ca are expected to be in the range from 0.45 to 0.55 fm (see, e.g., [72]).

We will make use of the model of Sec. III to illustrate the sensitivity of the double ratio to both parameters of a two-parameter Fermi distribution. For the proton distributions of ^{40}Ca and ^{48}Ca and the neutron distribution of ^{40}Ca we adopted fixed half-density radii of 4 fm and diffuseness parameters of 0.6 fm, which describe the GiBUU generated ones reasonably well. For the neutron distribution of ^{48}Ca the half-density radius $R_n(^{48}$Ca) and the skin depth $a_n(^{48}$Ca) were varied independently.
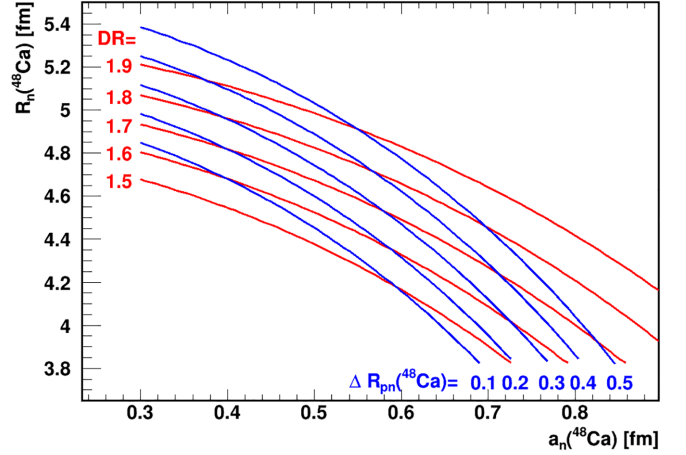

FIG. 10. Probing the dependence of the double ratio DR and the neutron skin thickness ΔR_{pn} on variations of the half-density radius R_n and the diffuseness a_n of the neutron density distribution in ^{48}Ca. Calculations were performed according to Sec. III with a two-parameter Fermi function as an anzatz for the density distributions of ^{48}Ca with half-density radius $R_n(^{48}$Ca) and diffuseness $a_n(^{48}$Ca). For the proton distributions of ^{40}Ca and ^{48}Ca and the neutron distribution of ^{40}Ca, fixed half-density radii of 4 fm and diffuseness of 0.6 fm were used. The plot shows isolines for the double ratio (blue) and neutron skin thickness of ^{48}Ca (red).

Figure 10 shows isolines for the double ratio (blue) and neutron skin thickness of ^{48}Ca (red) defined via the difference of the proton and neutron rms radii, in the $R_n(^{48}$Ca)-$a_n(^{48}$Ca) parameter space. A precise determination of the double ratio will determine a specific narrow monotonic relation between R_n and a_n in Fig. 10. Note that for a Fermi function the diffuseness parameter corresponds to the inverse of the slope at the half-density radius. Thus, without referring to a specific analytical shape of the density distributions, the slope (or its inverse) at the half-density radius $d\rho/dr|_{r=R_q}$, may provide a more general characterization of the diffuseness of theoretical predictions. Since, e.g., each model shown in Fig. 1 will mark a point in Fig. 10, the double ratio may serve as a sensitive test for the various models.

The fact that the blue and red isolines are not running parallel signals that the double ratio is not uniquely related to the rms radius of the neutrons but also depends on admixtures of higher moments. Indeed, the combination of the present method with other observables which probe different regions of the neutron skin, e.g., antiprotonic atoms [38], may enable a deeper view beyond the simple rms value on the neutron skin.

VI. EXPERIMENTAL ASPECTS AND OUTLOOK

The present GiBUU simulations focused on an incident antiproton momentum of 2.4 GeV/c. Of course, the beam momentum needs to be optimized with respect to, e.g., the production yields, experimental efficiency, and sensitivity. In particular, the $\Sigma^- \overline{\Lambda}$ pair production will be reduced at lower beam momenta. Preliminary results for the neon case at a lower momentum of 1.7 GeV/c have been presented earlier [73]. Due to the larger $\overline{p} + n$ cross section of

63 mb at an antiproton momentum 1.7 GeV/c, the schematic model of Sec. III predicts an increase of the double ratio by about 1.4% as compared to the case of 2.4 GeV/c. The GiBUU simulations (with improved statistics with respect to [73]) predict a double ratio of 1.440 ± 0.054 and hence a somewhat larger increase by $6.2 \pm 4.1\%$. However, the statistical uncertainty is still rather large due to the limited computing time. Though this explorative result suggests that the incident antiproton momentum has only a small effect on the double ratio, a systematic study with larger event samples is clearly desirable. It would be of interest to perform corresponding calculations with other transport model codes [74–80], also under the aspect of systematic model uncertainties.

The proposed method focuses on the total production ratios of $\Lambda \overline{\Lambda}$ and $\Sigma^- \overline{\Lambda}$ pairs. The masses of the Λ and $\overline{\Lambda}$ hyperons can be easily reconstructed by the charged decay channel. The identification of the $\Sigma^- \rightarrow \pi^- n$ decay channel, which dominates with 99.8%, will be more challenging. At $\overline{P}$ANDA, about 2.7% of the Σ^- tracks can be reconstructed by the microvertex detector. The Σ^- can be identified by a kinematic fit including the Σ^--π^- decay vertex and the associated hit of the neutron in the calorimeter. The reduced Σ^- mass resolution will of course increase the background for $\Sigma^- \overline{\Lambda}$ pairs. Nevertheless, in the double ratio, many systematic effects will cancel. Furthermore, $\overline{p}$-p and $\overline{p}$-d interactions will provide important points of reference.

At $\overline{P}$ANDA, reconstruction efficiencies of 30%, 30%, and 2% are expected for Λ, $\overline{\Lambda}$, and Σ^-, respectively [81]. Even with a moderate average interaction rate of 2×10^6 s^{-1}, the statistical precision shown in Table II, e.g., for calcium, can be reached in about half a day for each isotope. Although the additional background, particularly for the Σ^-, may require

somewhat larger measuring periods, this estimate demonstrates the large potential of this method for a precision study at an antiproton storage ring.

With the regular pellet target system of the $\overline{P}$ANDA setup, all noble gases can be employed. But even with a cleaning and recirculation system the operation with such isotopically enriched gaseous isotopes will be rather costly. Instead, with a filament target system similar to the one developed for the hyperatom studies at $\overline{P}$ANDA [82,83], many solid nuclear targets are also feasible. Note, that only a few milligrams of material is needed for such a target filaments. While we have focused in this work on the two double magic calcium isotopes, additional calcium isotopes or many other isotope chains, e.g., $^{58-64}$Ni [84], will therefore be experimentally accessible at a reasonable price, and with enrichment [85] and measuring times. For specific isotope pairs, where sufficient target material is available, also a measurement in a fixed target mode may be feasible, e.g,. making use of the antiproton beam at J-PARC [86].

Finally we note that an analogous method might also allow one to explore the evolution of the proton skin thickness in isotone chains. Combined with precise data on the proton distributions this might give access to the neutron distributions in proton rich isotones.

TABLE III. Published radii of protons and neutrons in ^{48}Ca which are shown in Fig. 1.

Method	Reference	R_p (fm)	R_n (fm)	ΔR_{pn} (fm)
10.8–16.3 MeV p elastic scattering	[90]	3.38	3.78 ± 0.09	0.39 ± 0.10
1044 MeV p elastic scattering	[13]	3.48	3.66	0.16 ± 0.023
1040 MeV p elastic scattering	[91]	3.38	3.54	0.16 ± 0.05
1040 MeV p scattering	[21]	3.41	$3.58 \pm 0.04 \pm 0.1$	$0.18 \pm 0.04 \pm 0.1$
800 MeV $\vec{p} + {}^{48}$Ca	[92]	3.376^a	3.561^a	0.18 ± 0.08
500–1040 MeV p scattering	[23]		3.436 ± 0.023	0.079 ± 0.023
$n + {}^{48}$Ca and $p + {}^{48}$Ca scattering	[93]			0.249 ± 0.023
$p + {}^{48}$Ca and ^{48}Ca $+ {}^{12}$C scattering	[20]			$0.158 \pm 0.023(\text{exp}) \pm 0.012(\text{mod})$
$p + {}^{48}$Ca and ^{48}Ca $+ {}^{12}$C scattering	[28]		3.43 ± 0.16	
166 MeV α elastic scattering	[94]	3.39	3.72 ± 0.12	0.33 ± 0.12
1370 MeV α elastic scattering	[95]	3.48	3.67 ± 0.05	0.19 ± 0.05
104 MeV α elastic scattering	[96]			0.17 ± 0.10
^{48}Ca $+ {}^{12}$C interaction cross section	[27]			0.197 ± 0.048
π^- and π^+ scattering	[97]			0.20 ± 0.09^a
π^- and π^+ scattering	[14,15]	3.32 ± 0.03	3.43 ± 0.03	0.11 ± 0.04
Analysis of antiprotonic atoms	[16]			$0.12^{+0.04}_{-0.08}$
Pionic atoms	[98]			0.13 ± 0.06
	[98]			0.16 ± 0.07
Electric dipole polarizability	[36]			0.17 ± 0.03
CREX	[52]			$0.121 \pm 0.026(\text{exp}) \pm 0.024(\text{mod})$

^{a}Assuming $R_p = R_n$ for ^{40}Ca.

TABLE IV. The neutron skin thickness $\Delta R_{np} = R_{\mathrm{rms}}(n) - R_{\mathrm{rms}}(p)$ of ^{208}Pb deduced by different experiments and analyses as shown in Fig. 1.

Method	Reference	ΔR_{pn} (fm)	Remark
Elastic p and n scattering at 40, 65, 200 MeV	[22]	0.17	
Elastic p scattering at 295 MeV	[18]	$0.211^{+0.054}_{-0.063}$	
Elastic p scattering at 650 MeV	[99,100]	0.20 ± 0.04	
$p + {}^{208}$Pb reaction cross section at 30–100 MeV	[26]	0.278 ± 0.035	
^{208}Pb $+ {}^{208}$Pb at LHC	[29]	0.217 ± 0.058	
Antiprotonic atoms	[101]	$0.16 \pm (0.02)_{\mathrm{stat}} \pm (0.04)_{\mathrm{syst}}$	
	[102]	0.21 ± 0.03	
	[103]	$0.20 \pm (0.04)_{\mathrm{exp}} \pm (0.04)_{\mathrm{theo}}$	Reanalysis of [101]
Pionic atoms	[98]	0.15 ± 0.08	
	[98]	0.14 ± 0.10	
π^+ reaction cross section	[98]	0.11 ± 0.06	$^{\mathrm{nat}}$Pb target
Strength of pigmy dipole resonance	[104]	0.18 ± 0.035	
	[33]	0.194 ± 0.024	
Electric dipole polarizability	[35]	$0.156^{+0.025}_{-0.021}$	
By $\vec{p}$ scattering at 295 MeV	[105]	$0.165 \pm (0.009)_{\mathrm{exp}} \pm (0.013)_{\mathrm{theo}} \pm (0.021)_{\mathrm{est}}$	
	[35,106]	0.168 ± 0.022	Reanalysis of [35]
Giant dipole resonance; 120 MeV α scattering	[31]	0.19 ± 0.09	See [32]
Giant dipole resonance; 196 MeV α scattering	[32,107]	0.12 ± 0.07	
Anti-analog giant dipole resonance	[108]	0.161 ± 0.042	
	[109,110]	$0.216 \pm (0.046)_{\mathrm{exp}} \pm (0.015)_{\mathrm{theo}}$	
Coherent π^0 production	[37]	0.15 ± 0.03 (stat.) $^{+0.01}_{-0.03}$(sys.)	
Parity violating e^- scattering	[50]	$0.33^{+0.16}_{-0.18}$	
Parity violating e^- scattering PREX 1+2	[51]	0.283 ± 0.071	
Tidal deformability from neutron star merger	[40]	$\leqslant 0.25$	Analysis of [41]
NICER	[111,112]	$\leqslant 0.31$	Analysis of [42]

DATA AVAILABILITY

The data supporting this study's findings are available within the article.

APPENDIX

Tables III and IV collect the values and references for the data displayed in Fig. 1.

[1] M. B. Tsang, J. R. Stone, F. Camera, P. Danielewicz, S. Gandolfi, K. Hebeler, C. J. Horowitz, J. Lee, W. G. Lynch, Z. Kohley, R. Lemmon, P. Möller, T. Murakami, S. Riordan, X. Roca-Maza, F. Sammarruca, A. W. Steiner, I. Vidaña, and S. J. Yennello, Constraints on the symmetry energy and neutron skins from experiments and theory, Phys. Rev. C **86**, 015803 (2012).

[2] M. Baldo and G. Burgio, The nuclear symmetry energy, Prog. Part. Nucl. Phys. **91**, 203 (2016).

[3] J. Piekarewicz and F. J. Fattoyev, Neutron-rich matter in heaven and on earth, Phys. Today **72**(7), 30 (2019).

[4] B. A. Brown, Neutron radii in nuclei and the neutron equation of state, Phys. Rev. Lett. **85**, 5296 (2000).

[5] C. J. Horowitz and J. Piekarewicz, Neutron star structure and the neutron radius of ^{208}Pb, Phys. Rev. Lett. **86**, 5647 (2001).

[6] S. Typel and B. A. Brown, Neutron radii and the neutron equation of state in relativistic models, Phys. Rev. C **64**, 027302 (2001).

[7] C. J. Horowitz and J. Piekarewicz, Neutron radii of ^{208}Pb and neutron stars, Phys. Rev. C **64**, 062802(R) (2001).

[8] F. Sammarruca and P. Liu, Neutron skin of ^{208}Pb and density dependence of the symmetry energy, Phys. Rev. C **79**, 057301 (2009).

[9] X. Roca-Maza, M. Brenna, B. K. Agrawal, P. F. Bortignon, G. Colo, L.-G. Cao, N. Paar, and D. Vretenar, Giant quadrupole resonances in ^{208}Pb, the nuclear symmetry energy, and the neutron skin thickness, Phys. Rev. C **87**, 034301 (2013).

[10] P.-G. Reinhard and W. Nazarewicz, Nuclear charge and neutron radii and nuclear matter: Trend analysis in skyrme

density-functional-theory approach, Phys. Rev. C **93**, 051303(R) (2016).

[11] M. Centelles, X. Roca-Maza, X. Viñas, and M. Warda, Nuclear symmetry energy probed by neutron skin thickness of nuclei, Phys. Rev. Lett. **102**, 122502 (2009).

[12] T. Suzuki, H. Geissel, O. Bochkarev, L. Chulkov, M. Golovkov, D. Hirata, H. Irnich, Z. Janas, H. Keller, T. Kobayashi, G. Kraus, G. Münzenberg, S. Neumaier, F. Nickel, A. Ozawa, A. Piechaczeck, E. Roeckl, W. Schwab, K. Sümmerer, K. Yoshida *et al.*, Neutron skin of Na isotopes studied via their interaction cross sections, Phys. Rev. Lett. **75**, 3241 (1995).

[13] G. Alkhazov, T. Bauer, R. Beurtey, A. Boudard, G. Bruge, A. Chaumeaux, P. Couvert, G. Cvijanovich, H. Duhm, J. Fontaine, D. Garreta, A. Kulikov, D. Legrand, J. Lugol, J. Saudinos, J. Thirion, and A. Vorobyov, Elastic and inelastic scattering of 1.044 GeV protons by ^{40}Ca, ^{42}Ca, ^{44}Ca, ^{48}Ca and ^{48}Ti, Nucl. Phys. A **274**, 443 (1976).

[14] K. G. Boyer, W. J. Braithwaite, W. B. Cottingame, S. J. Greene, L. E. Smith, C. F. Moore, C. L. Morris, H. A. Thiessen, G. S. Blanpied, G. R. Burleson, J. F. Davis, J. S. McCarthy, R. C. Minehart, and C. A. Goulding, Pion elastic and inelastic scattering from ^{40,42,44,48}Ca and ^{54}Fe, Phys. Rev. C **29**, 182 (1984).

[15] W. R. Gibbs and J.-P. Dedonder, Neutron radii of the calcium isotopes, Phys. Rev. C **46**, 1825 (1992).

[16] F. J. Hartmann, R. Schmidt, B. Ketzer, T. von Egidy, S. Wycech, R. Smolańczuk, T. Czosnyka, J. Jastrzebski, M. Kisieliński, P. Lubiński, P. Napiorkowski, L. Pieńkowski, A. Trzcińska, B. Kłos, K. Gulda, W. Kurcewicz, and E. Widmann, Nucleon density in the nuclear periphery determined with antiprotonic x rays: Calcium isotopes, Phys. Rev. C **65**, 014306 (2001).

[17] T. Yamaguchi, T. Suzuki, T. Ohnishi, F. Becker, M. Fukuda, H. Geissel, M. Hosoi, R. Janik, K. Kimura, T. Kuboki, S. Mandel, M. Matsuo, G. Münzenberg, S. Nakajima, T. Ohtsubo, A. Ozawa, A. Prochazka, M. Shindo, B. Sitár, P. Strmeň *et al.*, Nuclear matter radii of neutron-deficient Kr isotopes, Phys. Rev. C **77**, 034315 (2008).

[18] J. Zenihiro, H. Sakaguchi, T. Murakami, M. Yosoi, Y. Yasuda, S. Terashima, Y. Iwao, H. Takeda, M. Itoh, H. P. Yoshida, and M. Uchida, Neutron density distributions of ^{204,206,208}Pb deduced via proton elastic scattering at $E_p = 295$ MeV, Phys. Rev. C **82**, 044611 (2010).

[19] S. Mizutori, J. Dobaczewski, G. A. Lalazissis, W. Nazarewicz, and P.-G. Reinhard, Nuclear skins and halos in the mean-field theory, Phys. Rev. C **61**, 044326 (2000).

[20] S. Tagami, T. Wakasa, M. Takechi, J. Matsui, and M. Yahiro, Neutron skin in ^{48}Ca determined from $p + {}^{48}$Ca and ^{48}Ca $+ {}^{12}$C scattering, Results Phys. **33**, 105155 (2022).

[21] I. Brissaud and X. Campi, Determination of matter densities of Ca isotopes by 600 MeV and 1 GeV proton elastic scattering, Phys. Lett. B **86**, 141 (1979).

[22] S. Karataglidis, K. Amos, B. A. Brown, and P. K. Deb, Discerning the neutron density distribution of ^{208}Pb from nucleon elastic scattering, Phys. Rev. C **65**, 044306 (2002).

[23] B. C. Clark, L. J. Kerr, and S. Hama, Neutron densities from a global analysis of medium-energy proton-nucleus elastic scattering, Phys. Rev. C **67**, 054605 (2003).

[24] H. Sakaguchi and J. Zenihiro, Proton elastic scattering from stable and unstable nuclei—extraction of nuclear densities, Prog. Part. Nucl. Phys. **97**, 1 (2017).

[25] I. A. M. Abdul-Magead, E. Hamza, and B. Abu-Ibrahim, Neutron radii and neutron skin of neutron-rich nuclei deduced from proton-nucleus total reaction cross sections, J. Phys. G: Nucl. Part. Phys. **47**, 055103 (2020).

[26] S. Tagami, T. Wakasa, J. Matsui, M. Yahiro, and M. Takechi, Neutron skin thickness of ^{208}Pb determined from the reaction cross section for proton scattering, Phys. Rev. C **104**, 024606 (2021).

[27] M. Tanaka, M. Takechi, A. Homma, M. Fukuda, D. Nishimura, T. Suzuki, Y. Tanaka, T. Moriguchi, D. S. Ahn, A. Aimaganbetov, M. Amano, H. Arakawa, S. Bagchi, K.-H. Behr, N. Burtebayev, K. Chikaato, H. Du, S. Ebata, T. Fujii, N. Fukuda *et al.*, Swelling of doubly magic ^{48}Ca core in Ca isotopes beyond $N = 28$, Phys. Rev. Lett. **124**, 102501 (2020).

[28] I. A. M. Abdul-Magead and B. Abu-Ibrahim, Neutron skin of neutron-rich nuclei, Phys. Rev. C **105**, 014626 (2022).

[29] G. Giacalone, G. Nijs, and W. van der Schee, Determination of the neutron skin of ^{208}Pb from ultrarelativistic nuclear collisions, Phys. Rev. Lett. **131**, 202302 (2023).

[30] H. Lenske and P. Kienle, Probing matter radii of neutron-rich nuclei by antiproton scattering, Phys. Lett. B **647**, 82 (2007).

[31] A. Krasznahorkay, J. Bacelar, J. A. Bordewijk, S. Brandenburg, A. Buda, G. van 't Hof, M. A. Hofstee, S. Kato, T. D. Poelhekken, S. Y. van der Werf, A. van der Woude, M. N. Harakeh, and N. Kalantar-Nayestanaki, Excitation of the isovector giant dipole resonance by inelastic α scattering and the neutron skin of nuclei, Phys. Rev. Lett. **66**, 1287 (1991).

[32] A. Krasznahorkay, H. Akimune, A. van den Berg, N. Blasi, S. Brandenburg, M. Csatlós, M. Fujiwara, J. Gulyás, M. Harakeh, M. Hunyadi, M. de Huu, Z. Mate, D. Sohler, S. van der Werf, H. Wörtche, and L. Zolnai, Neutron-skin thickness in neutron-rich isotopes, Nucl. Phys. A **731**, 224 (2004).

[33] A. Carbone, G. Colò, A. Bracco, L.-G. Cao, P. F. Bortignon, F. Camera, and O. Wieland, Constraints on the symmetry energy and neutron skins from pygmy resonances in ^{68}Ni and ^{132}Sn, Phys. Rev. C **81**, 041301(R) (2010).

[34] A. Krasznahorkay, M. Fujiwara, P. van Aarle, H. Akimune, I. Daito, H. Fujimura, Y. Fujita, M. N. Harakeh, T. Inomata, J. Jänecke, S. Nakayama, A. Tamii, M. Tanaka, H. Toyokawa, W. Uijen, and M. Yosoi, Excitation of isovector spin-dipole resonances and neutron skin of nuclei, Phys. Rev. Lett. **82**, 3216 (1999).

[35] A. Tamii, I. Poltoratska, P. von Neumann-Cosel, Y. Fujita, T. Adachi, C. A. Bertulani, J. Carter, M. Dozono, H. Fujita, K. Fujita, K. Hatanaka, D. Ishikawa, M. Itoh, T. Kawabata, Y. Kalmykov, A. M. Krumbholz, E. Litvinova, H. Matsubara, K. Nakanishi, R. Neveling *et al.*, Complete electric dipole response and the neutron skin in ^{208}Pb, Phys. Rev. Lett. **107**, 062502 (2011).

[36] J. Birkhan, M. Miorelli, S. Bacca, S. Bassauer, C. A. Bertulani, G. Hagen, H. Matsubara, P. von Neumann-Cosel, T. Papenbrock, N. Pietralla, V. Y. Ponomarev, A. Richter, A. Schwenk, and A. Tamii, Electric dipole polarizability of ^{48}Ca and implications for the neutron skin, Phys. Rev. Lett. **118**, 252501 (2017).

[37] C. M. Tarbert *et al.* (Crystal Ball at MAMI and A2 Collaboration), Neutron skin of ^{208}Pb from coherent pion photoproduction, Phys. Rev. Lett. **112**, 242502 (2014).

[38] A. Trzcińska, J. Jastrzebski, P. Lubiński, F. J. Hartmann, R. Schmidt, T. von Egidy, and B. Kłos, Neutron density distributions deduced from antiprotonic atoms, Phys. Rev. Lett. **87**, 082501 (2001).

[39] C. Horowitz, K. Kumar, and R. Michaels, Electroweak measurements of neutron densities in CREX and PREX at JLab, USA, Eur. Phys. J. A **50**, 48 (2014).

[40] F. J. Fattoyev, J. Piekarewicz, and C. J. Horowitz, Neutron skins and neutron stars in the multimessenger era, Phys. Rev. Lett. **120**, 172702 (2018).

[41] B. Abbott *et al.* (LIGO Scientific Collaboration and Virgo Collaboration), GW170817: Observation of gravitational waves from a binary neutron star inspiral, Phys. Rev. Lett. **119**, 161101 (2017).

[42] B. T. Reed, F. J. Fattoyev, C. J. Horowitz, and J. Piekarewicz, Implications of PREX-2 on the equation of state of neutron-rich matter, Phys. Rev. Lett. **126**, 172503 (2021).

[43] G. A. Miller, Coherent-nuclear pion photoproduction and neutron radii, Phys. Rev. C **100**, 044608 (2019).

[44] A. Ekström, G. R. Jansen, K. A. Wendt, G. Hagen, T. Papenbrock, B. D. Carlsson, C. Forssén, M. Hjorth-Jensen, P. Navrátil, and W. Nazarewicz, Accurate nuclear radii and binding energies from a chiral interaction, Phys. Rev. C **91**, 051301(R) (2015).

[45] J. E. Sobczyk, B. Acharya, S. Bacca, and G. Hagen, *Ab initio* computation of the longitudinal response function in ^{40}Ca, Phys. Rev. Lett. **127**, 072501 (2021).

[46] K. Hebeler, Three-nucleon forces: Implementation and applications to atomic nuclei and dense matter, Phys. Rep. **890**, 1 (2021).

[47] C. McIlroy, C. Barbieri, T. Inoue, T. Doi, and T. Hatsuda, Doubly magic nuclei from lattice QCD forces at $M_{ps} = 469 \, \text{MeV}/c^2$, Phys. Rev. C **97**, 021303(R) (2018).

[48] T. Miyagi, T. Abe, M. Kohno, P. Navrátil, R. Okamoto, T. Otsuka, N. Shimizu, and S. R. Stroberg, Ground-state properties of doubly magic nuclei from the unitary-model-operator approach with chiral two- and three-nucleon forces, Phys. Rev. C **100**, 034310 (2019).

[49] C. H. Hyun, Neutron skin thickness of ^{48}Ca, ^{132}Sn, and ^{208}Pb with KIDS density functional, New Phys.: Sae Mulli **72**, 371 (2022).

[50] S. Abrahamyan *et al.* (PREX Collaboration), Measurement of the neutron radius of ^{208}Pb through parity violation in electron scattering, Phys. Rev. Lett. **108**, 112502 (2012).

[51] D. Adhikari *et al.* (PREX Collaboration), Accurate determination of the neutron skin thickness of ^{208}Pb through parity-violation in electron scattering, Phys. Rev. Lett. **126**, 172502 (2021).

[52] D. Adhikari *et al.* (CREX Collaboration), Precision determination of the neutral weak form factor of ^{48}Ca, Phys. Rev. Lett. **129**, 042501 (2022).

[53] M. C. Atkinson, M. H. Mahzoon, M. A. Keim, B. A. Bordelon, C. D. Pruitt, R. J. Charity, and W. H. Dickhoff, Dispersive optical model analysis of ^{208}Pb generating a neutron-skin prediction beyond the mean field, Phys. Rev. C **101**, 044303 (2020).

[54] C. D. Pruitt, R. J. Charity, L. G. Sobotka, M. C. Atkinson, and W. H. Dickhoff, Systematic matter and binding-energy

[55] P.-G. Reinhard, X. Roca-Maza, and W. Nazarewicz, Combined theoretical analysis of the parity-violating asymmetry for ^{48}Ca and ^{208}Pb, Phys. Rev. Lett. **129**, 232501 (2022).

[56] O. Buss, T. Gaitanos, K. Gallmeister, H. van Hees, M. Kaskulov, O. Lalakulich, A. Larionov, T. Leitner, J. Weil, and U. Mosel, Transport-theoretical description of nuclear reactions, Phys. Rep. **512**, 1 (2012).

[57] R. L. Workman *et al.* (Particle Data Group), Review of particle physics, Prog. Theor. Exp. Phys. **2022**, 083C01 (2022).

[58] G. A. Lalazissis, J. König, and P. Ring, New parametrization for the Lagrangian density of relativistic mean field theory, Phys. Rev. C **55**, 540 (1997).

[59] H. D. Vries, C. D. Jager, and C. D. Vries, Nuclear charge-density-distribution parameters from elastic electron scattering, At. Data Nucl. Data Tables **36**, 495 (1987).

[60] I. Angeli and K. Marinova, Table of experimental nuclear ground state charge radii: An update, At. Data Nucl. Data Tables **99**, 69 (2013).

[61] R. F. Garcia Ruiz, M. L. Bissell, K. Blaum, A. Ekström, N. Frömmgen, G. Hagen, M. Hammen, K. Hebeler, J. D. Holt, G. R. Jansen, M. Kowalska, K. Kreim, W. Nazarewicz, R. Neugart, G. Neyens, W. Nörtershäuser, T. Papenbrock, J. Papuga, A. Schwenk, J. Simonis *et al.*, Unexpectedly large charge radii of neutron-rich calcium isotopes, Nat. Phys. **12**, 594 (2016).

[62] G. Lalazissis, S. Karatzikos, R. Fossion, D. P. Arteaga, A. Afanasjev, and P. Ring, The effective force NL3 revisited, Phys. Lett. B **671**, 36 (2009).

[63] S. Malbrunot-Ettenauer, S. Kaufmann, S. Bacca, C. Barbieri, J. Billowes, M. L. Bissell, K. Blaum, B. Cheal, T. Duguet, R. F. Garcia Ruiz, W. Gins, C. Gorges, G. Hagen, H. Heylen, J. D. Holt, G. R. Jansen, A. Kanellakopoulos, M. Kortelainen, T. Miyagi, P. Navrátil *et al.*, Nuclear charge radii of the nickel isotopes $^{58-68,70}$Ni, Phys. Rev. Lett. **128**, 022502 (2022).

[64] D. Atanasov, D. Beck, K. Blaum, C. Borgmann, R. Cakirli, T. Eronen, S. George, F. Herfurth, A. Herlert, M. Kowalska, S. Kreim, Y. Litvinov, D. Lunney, V. Manea, D. Neidherr, M. Rosenbusch, L. Schweikhard, F. Wienholtz, R. Wolf, and K. Zuber, Precision mass measurements of cesium isotopes—new entries in the ISOLTRAP chronicles, J. Phys. G: Nucl. Part. Phys. **44**, 044004 (2017).

[65] A. B. Larionov, I. A. Pshenichnov, I. N. Mishustin, and W. Greiner, Antiproton-nucleus collisions simulation within a kinetic approach with relativistic mean fields, Phys. Rev. C **80**, 021601(R) (2009).

[66] A. B. Larionov, T. Gaitanos, and U. Mosel, Kaon and hyperon production in antiproton-induced reactions on nuclei, Phys. Rev. C **85**, 024614 (2012).

[67] F. Grümmer, B. Chen, Z. Ma, and S. Krewald, Bulk properties of light deformed nuclei derived from a medium-modified meson-exchange interaction, Phys. Lett. B **387**, 673 (1996).

[68] R. Panda, M. Sharma, and S. Patra, Nuclear structure and reaction properties of Ne, Mg and Si isotopes with RMF densities, Mod. Phys. Lett. A **29**, 1450013 (2014).

[69] A. J. Miller, K. Minamisono, A. Klose, D. Garand, C. Kujawa, J. D. Lantis, Y. Liu, B. Maaß, P. F. Mantica, W. Nazarewicz, W. Nötershäuser, S. V. Pineda, P.-G. Reinhard, D. M. Rossi, F. Sommer, C. Sumithrarachchi, A. Teigelhöfer, and J. Watkins,

Proton superfluidity and charge radii in proton-rich calcium isotopes, Nat. Phys. **15**, 432 (2019).

[70] H. Emrich, G. Fricke, G. Mallot, H. Miska, H.-G. Sieberling, J. Cavedon, B. Frois, and D. Goutte, Radial distribution of nucleons in the isotopes ^{48,40}Ca, Nucl. Phys. A **396**, 401 (1983).

[71] P. E. Hodgson, Nuclear matter distributions, Hyperfine Interact. **74**, 75 (1992).

[72] W. Horiuchi, Single-particle decomposition of nuclear surface diffuseness, Prog. Theor. Exp. Phys. **2021**, 123D01 (2021).

[73] J. Pochodzalla, S. Bleser, A. S. Lorente, M. M. Rojo, M. Steinen, for the PANDA Collaboration, J. Gerl, J. Kojouharova, and I. Kojouharov, Many facets of strangeness nuclear physics with stored antiprotons, JPS Conf. Proc. **17**, 091002 (2017).

[74] J. Hirtz, J.-C. David, A. Boudard, J. Cugnon, S. Leray, I. Leya, J. L. Rodríguez-Sánchez, and G. Schnabel, Strangeness production in the new version of the Liège intranuclear cascade model, Phys. Rev. C **101**, 014608 (2020).

[75] J. L. Rodríguez-Sánchez, J. Cugnon, J.-C. David, J. Hirtz, A. Kelić-Heil, and S. Leray, Hypernuclei formation in spallation reactions by coupling the Liège intranuclear cascade model to the deexcitation code ABLA, Phys. Rev. C **105**, 014623 (2022).

[76] G.-C. Yong, A direct probe of Λ potential in nuclear medium, Phys. Lett. B **853**, 138662 (2024).

[77] W. Ehehalt and W. Cassing, Relativistic transport approach for nucleus-nucleus collisions from SIS to SPS energies, Nucl. Phys. A **602**, 449 (1996).

[78] J. Geiss, W. Cassing, and C. Greiner, Strangeness production in the hsd transport approach from SIS to SPS energies, Nucl. Phys. A **644**, 107 (1998).

[79] C. Hartnack, H. Oeschler, Y. Leifels, E. L. Bratkovskaya, and J. Aichelin, Strangeness production close to the threshold in proton–nucleus and heavy-ion collisions, Phys. Rep. **510**, 119 (2012).

[80] J. Aichelin, E. Bratkovskaya, A. Le Fèvre, V. Kireyeu, V. Kolesnikov, Y. Leifels, V. Voronyuk, and G. Coci, Parton-hadron-quantum-molecular dynamics: A novel microscopic n-body transport approach for heavy-ion collisions, dynamical cluster formation, and hypernuclei production, Phys. Rev. C **101**, 044905 (2020).

[81] F. Schupp, Study of antihyperon pairs in nuclei at $\overline{P}$ANDA, Ph.D. thesis, Johannes Gutenberg-Universität Mainz (unpublished).

[82] M. Steinen, Feasibility studies for the high precision X-ray spectroscopy of heavy Ξ^- hyperatoms at $\overline{P}$ANDA using the PANda GErmanium Array PANGEA, Ph.D. thesis, Johannes Gutenberg-Universität Mainz, 2020.

[83] F. Schupp, M. Bölting, P. Achenbach, S. Bleser, J. Pochodzalla, and M. Steinen, An infrared light-guide based target positioning system for operation in a harsh environment, Nucl. Instrum. Methods Phys. Res. Sect. A **1056**, 168684 (2023).

[84] J. T. Zhang, X. L. Tu, P. Sarriguren, K. Yue, Q. Zeng, Z. Y. Sun, M. Wang, Y. H. Zhang, X. H. Zhou, and Y. A. Litvinov, Systematic trends of neutron skin thickness versus relative neutron excess, Phys. Rev. C **104**, 034303 (2021).

[85] Institut für Seltene Erden und Metalle AG, Price list of electromagnetically separated isotopes (2023), https://institut-seltene-erden.de/unser-service-2/metall-preise/preise-fuer-stabile-isotope/.

[86] K. Suzuki, The $\overline{p}$ physics opportunities at the j-parc hadron facility, in Fourth international workshop on the extension project for the J-PARC hadron experimental facility (HEF-ex) (2024), https://kds.kek.jp/event/46965/contributions/.

[87] M. Christiansen, F. Schupp, P. Achenbach, M. Bölting, J. Pochodzalla, and M. Steinen, Exploring the neutron skin by hyperon-antihyperon production in antiproton-nucleus interactions, EPJ Web Conf. **271**, 02011 (2022).

[88] M. Christiansen, Einfluss der Neutronenhaut auf die Produktion von Hyperon-Anthyperon-Paaren bei Antiproton-Kern-Stößen, Bachelor's thesis, Johannes Gutenberg-Universität Mainz, 2022.

[89] MOGON II high performance computing, https://hpc.uni-mainz.de/.

[90] J. Lombardi, R. Boyd, R. Arking, and A. Robbins, Nuclear sizes in ^{40,44,48}Ca, Nucl. Phys. A **188**, 103 (1972).

[91] A. Chaumeaux, V. Layly, and R. Schaeffer, Neutron densities from 1 GeV proton scattering, Phys. Lett. B **72**, 33 (1977).

[92] G. Igo, G. Adams, T. Bauer, G. Pauletta, C. Whitten, A. Wreikat, G. Hoffmann, G. Blanpied, W. Coker, C. Harvey, R. Liljestrand, L. Ray, J. Spencer, H. Thiessen, C. Glashausser, N. Hintz, M. Oothoudt, H. Nann, K. Seth, B. Wood *et al.*, Elastic differential cross sections and analyzing powers for $p + ^{40,42,44,48}$Ca at 0.8 GeV, Phys. Lett. B **81**, 151 (1979).

[93] M. H. Mahzoon, M. C. Atkinson, R. J. Charity, and W. H. Dickhoff, Neutron skin thickness of ^{48}Ca from a nonlocal dispersive optical-model analysis, Phys. Rev. Lett. **119**, 222503 (2017).

[94] I. Brissaud, Y. Le Bornec, B. Tatischeff, L. Bimbot, M. Brussel, and G. Duhamel, Détermination du rayon de la distribution de neutrons de certains noyaux par l'étude de la diffusion élastique de particules alpha de 166 mev, Nucl. Phys. A **191**, 145 (1972).

[95] G. Alkhazov, T. Bauer, R. Bertini, L. Bimbot, O. Bing, A. Boudard, G. Bruge, H. Catz, A. Chaumeaux, P. Couvert, J. Fontaine, F. Hibou, G. Igo, J. Lugol, and M. Matoba, Elastic and inelastic scattering of 1.37 GeV α-particles from ^{40,42,44,48}Ca, Nucl. Phys. A **280**, 365 (1977).

[96] E. Friedman, H. J. Gils, H. Rebel, and Z. Majka, ^{48}Ca - ^{40}Ca radius difference from elastic scattering of 104-MeV α particles, Phys. Rev. Lett. **41**, 1220 (1978).

[97] M. J. Jakobson, G. R. Burleson, J. R. Calarco, M. D. Cooper, D. C. Hagerman, I. Halpern, R. H. Jeppeson, K. F. Johnson, L. D. Knutson, R. E. Marrs, H. O. Meyer, and R. P. Redwine, Neutron radii of calcium isotopes from pion total cross section measurements, Phys. Rev. Lett. **38**, 1201 (1977).

[98] E. Friedman, Neutron skins of ^{208}Pb and ^{48}Ca from pionic probes, Nucl. Phys. A **896**, 46 (2012).

[99] V. E. Starodubsky and N. M. Hintz, Extraction of neutron densities from elastic proton scattering by ^{206,207,208}Pb at 650 MeV, Phys. Rev. C **49**, 2118 (1994).

[100] A. M. Mack, N. M. Hintz, D. Cook, M. A. Franey, J. Amann, M. Barlett, G. W. Hoffmann, G. Pauletta, D. Ciskowski, and M. Purcell, Proton scattering by ^{206,207,208}Pb at 650 MeV: Phenomenological analysis, Phys. Rev. C **52**, 291 (1995).

[101] B. Kłos, A. Trzcińska, J. Jastrzebski, T. Czosnyka, M. Kisieliński, P. Lubiński, P. Napiorkowski, L. Pieńkowski, F. J. Hartmann, B. Ketzer, P. Ring, R. Schmidt, T. von Egidy, R. Smolańczuk, S. Wycech, K. Gulda, W. Kurcewicz, E. Widmann, and B. A. Brown, Neutron density distributions

from antiprotonic ^{208}Pb and ^{209}Bi atoms, Phys. Rev. C **76**, 014311 (2007).

[102] S. Wycech, F. J. Hartmann, J. Jastrzébski, B. Kłos, A. Trzcińska, and T. von Egidy, Nuclear surface studies with antiprotonic atom x rays, Phys. Rev. C **76**, 034316 (2007).

[103] B. A. Brown, G. Shen, G. C. Hillhouse, J. Meng, and A. Trzcińska, Neutron skin deduced from antiprotonic atom data, Phys. Rev. C **76**, 034305 (2007).

[104] A. Klimkiewicz *et al.* (LAND Collaboration), Nuclear symmetry energy and neutron skins derived from pygmy dipole resonances, Phys. Rev. C **76**, 051603(R) (2007).

[105] A. Tamii, P. von Neumann-Cosel, and I. Poltoratska, Electric dipole response of ^{208}Pb from proton inelastic scattering: Constraints on neutron skin thickness and symmetry energy, Eur. Phys. J. A **50**, 28 (2014).

[106] J. Piekarewicz, B. K. Agrawal, G. Colò, W. Nazarewicz, N. Paar, P.-G. Reinhard, X. Roca-Maza, and D. Vretenar, Electric dipole polarizability and the neutron skin, Phys. Rev. C **85**, 041302(R) (2012).

[107] M. Csatlós, A. Krasznahorkay, D. Sohler, A. M. van den Berg, N. Blasi, J. Gulyás, M. N. Harakeh, M. Hunyadi, M. A. de Huu, Z. Máté, S. Y. van der Werf, H. J. Wörtche, and L. Zolnai, Measurement of neutron-skin thickness in ^{208}Pb by excitation of the GDR via inelastic α-scattering, Nucl. Phys. A **719**, C304 (2003).

[108] A. Krasznahorkay, N. Paar, D. Vretenar, and M. Harakeh, Neutron-skin thickness of ^{208}Pb from the energy of the anti-analogue giant dipole resonance, Phys. Scr. **T154**, 014018 (2013).

[109] J. Yasuda, T. Wakasa, M. Okamoto, M. Dozono, K. Hatanaka, M. Ichimura, S. Kuroita, Y. Maeda, T. Noro, Y. Sakemi, M. Sasano, and K. Yako, Extraction of antianalog giant dipole resonance and neutron skin thickness for ^{208}Pb, Prog. Theor. Exp. Phys. **2013**, 063D02 (2013).

[110] T. Wakasa, M. Okamoto, M. Dozono, K. Hatanaka, M. Ichimura, S. Kuroita, Y. Maeda, H. Miyasako, T. Noro, T. Saito, Y. Sakemi, T. Yabe, and K. Yako, Complete sets of polarization transfer observables for the ^{208}Pb($\vec{p}$, $\vec{n}$) reaction at 296 MeV and Gamow-Teller and spin-dipole strengths for ^{208}Pb, Phys. Rev. C **85**, 064606 (2012).

[111] T. E. Riley, A. L. Watts, S. Bogdanov, P. S. Ray, R. M. Ludlam, S. Guillot, Z. Arzoumanian, C. L. Baker, A. V. Bilous, D. Chakrabarty, K. C. Gendreau, A. K. Harding, W. C. G. Ho, J. M. Lattimer, S. M. Morsink, and T. E. Strohmayer, A *NICER* view of PSR j0030+0451: Millisecond pulsar parameter estimation, Astrophys. J. **887**, L21 (2019).

[112] M. C. Miller, F. K. Lamb, A. J. Dittmann, S. Bogdanov, Z. Arzoumanian, K. C. Gendreau, S. Guillot, A. K. Harding, W. C. G. Ho, J. M. Lattimer, R. M. Ludlam, S. Mahmoodifar, S. M. Morsink, P. S. Ray, T. E. Strohmayer, K. S. Wood, T. Enoto, R. Foster, T. Okajima, G. Prigozhin *et al.*, PSR j0030+0451 mass and radius from *NICER* data and implications for the properties of neutron star matter, Astrophys. J. **887**, L24 (2019).